

# The Harmonic Pitching NACA 0018 Airfoil in Low Reynolds Number Flow

Krzysztof Rogowski<sup>1\*</sup>, Maciej Śledziewski<sup>1</sup> and Jan Michna<sup>1</sup>

<sup>1\*</sup>Institute of Aeronautics and Applied Mechanics, Warsaw University of Technology, Nowowiejska 24, Warsaw, 00-665, Poland.

\*Corresponding author(s). E-mail(s): [krzysztof.rogowski@pw.edu.pl](mailto:krzysztof.rogowski@pw.edu.pl);  
Contributing authors: [maciej.sledziewski.stud@pw.edu.pl](mailto:maciej.sledziewski.stud@pw.edu.pl);  
[jan.michna.dokt@pw.edu.pl](mailto:jan.michna.dokt@pw.edu.pl);

## Abstract

This study investigates the aerodynamic performance of the symmetric NACA 0018 airfoil under harmonic pitching motions at low Reynolds numbers, a regime characterized by the presence of laminar separation bubbles and their impact on aerodynamic forces. The analysis encompasses oscillation frequencies of 1 Hz, 2 Hz, and 13.3 Hz, with amplitudes of 4° and 8°, along with steady-state simulations conducted for angles of attack up to 20° to validate the numerical model.

The results reveal that the Transition SST turbulence model provides improved predictions of aerodynamic forces at higher Reynolds numbers but struggles at lower Reynolds numbers, where laminar flow effects dominate. The inclusion of the 13.3 Hz frequency, relevant to Darrieus vertical-axis wind turbines, demonstrates the model's effectiveness in capturing dynamic hysteresis loops and reduced oscillations, contrasting with the  $k - \omega$  SST model. Comparisons with XFOIL further highlight challenges in accurately modeling laminar-to-turbulent transitions and dynamic flow phenomena.

These findings offer valuable insights into the aerodynamic behavior of thick airfoils under low Reynolds number conditions and contribute to advancing the understanding of turbulence modeling, particularly in applications involving vertical-axis wind turbines.

**Keywords:** Harmonic pitching, NACA 0018 airfoil, Low Reynolds number, Laminar separation bubbles, Transition SST turbulence model, Aerodynamic forces, Computational fluid dynamics, Unsteady aerodynamics

# 1 Introduction

In recent years, there has been growing interest in micro air vehicles (MAVs), driven by advancements in electronics and energy storage technologies. These MAVs hold significant potential for military applications, particularly in environments where the risk to human life is high. Recently, a Japanese research group proposed aircraft-like devices specifically designed for Mars exploration. The low weight and small size of these devices, combined with the need for low-speed cruising, require them to operate in environments characterized by very low Reynolds numbers, typically ranging from  $10^3$  to  $10^5$  [1], [2], [3], [4] and thus their dynamics significantly differs from conventional UAVs [5].

Another category of devices operating within a similar Reynolds number range includes small-scale wind turbines used in wind tunnel experiments. These turbines often have rotor diameters of one meter or smaller [6], [7]. Results obtained from such experiments are frequently scaled up to predict the performance of full-scale wind turbines, which can reach diameters of several hundred meters [8], [9]. Both propeller blades and wind turbine blades operating in unsteady inflow conditions are subject to oscillating loads and fluctuating angles of attack. For vertical-axis wind turbines (VAWTs), these oscillations are inherent and occur continuously during operation [10].

In low Reynolds number flows, laminar boundary layer separation occurs, which, through transition to turbulence, leads to the formation of laminar separation bubbles. The size of these bubbles can vary depending on the angle of attack and the Reynolds number, both of which influence the characteristics of flow separation [11], [12].

Generally, laminar separation bubbles can be classified into two types: short and long. Short bubbles decrease in length with increasing angle of attack and can cause significant flow instabilities. The study of these phenomena, however, is time-consuming and computationally demanding, as it often requires advanced numerical approaches such as Direct Numerical Simulation (DNS) or Large-Eddy Simulation (LES), typically performed on supercomputers [1], [13]. In recent years, several studies have employed both Large-Eddy Simulation (LES) and Direct Numerical Simulation (DNS). Due to the significant computational costs, these studies have primarily focused on thin airfoils. The results confirm the formation of short laminar separation bubbles at low Reynolds numbers and their impact on the nonlinearity of lift forces. However, the current state of knowledge still does not fully explain the causes of these nonlinearities.

One of the alternative methods for studying transition phenomena in low Reynolds number flows involves the use of modern models designed to capture the laminar-to-turbulent transition. Prior to the introduction of transition turbulence models, engineers primarily relied on turbulence models that treated the entire boundary layer as fully turbulent. Traditional turbulence models, such as those from the  $k-\omega$  or  $k-\epsilon$  family, fail to predict the nonlinear behavior of  $C_L$  below the critical angle of attack [14]. For applications in aeronautics, where Reynolds numbers typically reach several million or higher, neglecting the transition effects is often sufficient due to the dominance of turbulent boundary layers. One reason for the omission of transition effects in traditional turbulence models is the complexity and variability of transition mechanisms. Another key limitation lies in the absence of appropriate methods to describe

transition flows, including both linear and nonlinear effects, within the framework of Reynolds-averaged Navier–Stokes (RANS) equations.

Among the more recent advancements in modeling transition phenomena is the correlation-based  $\gamma - Re_\theta$  model, also known as the Transition SST turbulence model [15], [16]. This model predicts transition based on local flow conditions by solving transport equations that account for these conditions. In contrast, earlier transition models, such as the  $e^N$  method proposed by Smith and Gamberoni [17], relied on global flow parameters and proved challenging to implement in modern, general-purpose CFD software. While these older models could yield reasonable transition predictions for airfoil analysis in homogeneous flows, they were less effective for more complex cases.

Several studies have validated the effectiveness of the Transition SST turbulence model in capturing transition phenomena at low Reynolds numbers. Melani et al. [14] compiled a wide range of experimental and numerical data on the aerodynamic performance of the NACA 0018 airfoil at low and moderate Reynolds numbers. Their findings reveal that as the Reynolds number decreases, the discrepancies in aerodynamic force predictions increase, particularly in the range of Reynolds numbers from 40,000 to 160,000. Melani et al. [14] also provided lift force characteristics for a Reynolds number of 150,000, obtained using the Transition SST model. These results, which are also available in [18], show excellent agreement with experimental data for angles of attack up to 6 degrees.

A significant challenge for the Transition SST model lies in accurately estimating the dynamic characteristics of the pitching NACA 0018 airfoil under very low Reynolds number conditions.

Theodorsen and Glauert made groundbreaking contributions to the understanding of unsteady aerodynamics, particularly for pitching airfoils [19], [20], [21]. They provided foundational insights into the behavior of two-dimensional harmonically oscillating airfoils in inviscid and incompressible flows subjected to small disturbances. Theodorsen’s analytical framework remains a key reference for the performance analysis of both fixed-wing and rotating-wing systems, serving as a basis for further advancements in unsteady aerodynamics.

Theodorsen’s theory has several important limitations: it does not account for flow viscosity, is tailored specifically for thin airfoils, and lacks the capability to predict drag forces. Furthermore, at low Reynolds numbers, flows tend to separate prematurely, even at modest angles of attack, which further restricts the theory’s applicability in such conditions. Despite these limitations, Theodorsen’s framework has been adapted to address various aerodynamic challenges, including sudden changes in angle of attack, sinusoidal gust responses, and the dynamics of returning wakes [22].

A key parameter for characterizing the behavior of an airfoil undergoing harmonic oscillations is the reduced frequency,  $k$ , defined as  $k = \frac{\omega c}{2V_0}$ , where  $c$  represents the chord length,  $V_0$  is the free-stream velocity, and  $\omega$  denotes the angular frequency of oscillation. When  $k = 0$ , the flow is considered entirely steady. For cases where unsteady effects are minimal, the reduced frequency lies in the range  $0 < k \leq 0.05$ . As  $k$  increases beyond 0.05, the flow transitions into the unsteady regime, and when  $k \geq 0.2$ , the flow is classified as highly unsteady, exhibiting significant deviations from quasi-steady behavior [23], [21].

Theoretical studies similar to those presented in this paper, focusing on a two-dimensional flat plate undergoing harmonic pitching oscillations (without plunging motion) about the quarter-chord, within a Reynolds number range of  $10^4 - 10^5$  and reduced frequencies between 0.001 and 0.3, were conducted by Badrya et al. [21]. The authors aimed to analyze the influence of viscosity on flow behavior and the generation of aerodynamic forces and moments. Additionally, they compared the results obtained for the flat plate with those for the thin NACA 0012 airfoil. Badrya et al. [21] also employed Theodorsen’s theory and observed significant discrepancies between its predictions and numerical results. These differences were particularly pronounced at low Reynolds numbers and were attributed to the theory’s inability to account for viscous effects. Furthermore, in the case of the NACA 0012 airfoil, it was found that this airfoil fails to generate sufficient pressure differences between the upper and lower surfaces, resulting in very low maximum lift coefficients.

Another notable study in the field of pitching motions at low Reynolds numbers was conducted by Stevens and Babinsky [24]. They investigated the behavior of a flat plate undergoing harmonic pitching oscillations with a high reduced frequency of 0.394 at a Reynolds number of 20,000. Their work combined experimental measurements with a reduced-order model that incorporated both circulation and vortex advection velocities as informed by the experimental data. This approach highlighted the significance of including unsteady aerodynamic effects when modeling such flows.

Moreover, Brunton and Rowley [25] demonstrated the applicability of Theodorsen’s classical theory [19] in predicting lift for attached flows during pure pitching motion. They concluded that for scenarios dominated by non-circulatory and circulatory effects, Theodorsen’s model provides a reasonable approximation, despite its limitations in capturing vortex dynamics. These studies collectively underscore the complexity of flow behavior at low Reynolds numbers and the challenges in bridging theoretical predictions with experimental results.

The interplay between geometry, kinematics, Reynolds numbers, and three-dimensional effects significantly influences the aerodynamic forces and flow structures around pitching and plunging flat plates at low Reynolds numbers, as demonstrated by Kang et al. [26]. Shallow- and deep-stall motions reveal dominant geometric effects, such as massive leading-edge separation on sharp-edged flat plates, which overshadow viscosity-related influences. Compared to blunter airfoils like the SD7003, flat plates exhibit earlier and stronger leading-edge vortex formation, resulting in enhanced lift and drag characteristics under similar conditions.

Moriche et al. [27] analyzed the stability of a plunging and pitching wing with an infinite aspect ratio at low Reynolds numbers. By varying the mean pitch angle and phase shift between pitching and plunging, they identified cases producing different aerodynamic forces and wake structures. Notably, one configuration exhibited a period doubling phenomenon and was linearly unstable, leading to a fully three-dimensional wake downstream. Despite this, the aerodynamic forces in three-dimensional simulations remained consistent with their two-dimensional counterparts.

The current study aims to bridge the knowledge gap in understanding the aerodynamic performance of thick airfoils, such as the NACA 0018, under low Reynolds number regimes with harmonic pitching motions. Specifically, the research focuses on

a pitching motion frequency of 13.3 Hz, motivated by the operational characteristics of Darrieus vertical-axis wind turbines (VAWTs). These turbines, including the rotor tested in the TU Delft wind tunnel [6], provide a unique context where laminar separation bubbles and oscillatory aerodynamic forces significantly influence performance. By employing advanced turbulence modeling techniques, such as the  $\gamma - Re_\theta$  transition model and the  $k - \omega$  SST model, and comparing the numerical predictions against experimental data, this study seeks to unravel the dynamics of hysteresis loops, laminar separation bubbles, and turbulence effects. The findings contribute to a deeper understanding of aerodynamic force oscillations and their dependency on Reynolds numbers, thereby supporting the optimization of thick airfoils for a wide range of engineering applications.

## 2 The harmonic pitching NACA 0018 airfoil

The concept of pure pitching motion for the NACA 0018 airfoil is illustrated in Fig. 1. The symmetric NACA 0018 airfoil oscillates harmonically according to a sinusoidal function (also shown in the figure) about a pivot point located on the chord at a distance of  $c/4$  from the leading edge. The chord length, denoted as  $c$ , is also depicted in the sketch and measures 6 cm.

The oscillation frequency is denoted by  $f$ , with the corresponding period  $T$ , angular frequency  $\omega$ , and amplitude  $A$ . The origin of the coordinate system is defined at the quarter-chord point, measured from the leading edge. The constant pitch angle is represented by  $\alpha_0$ . In this study, only cases where  $\alpha_0 = 0^\circ$  are considered.

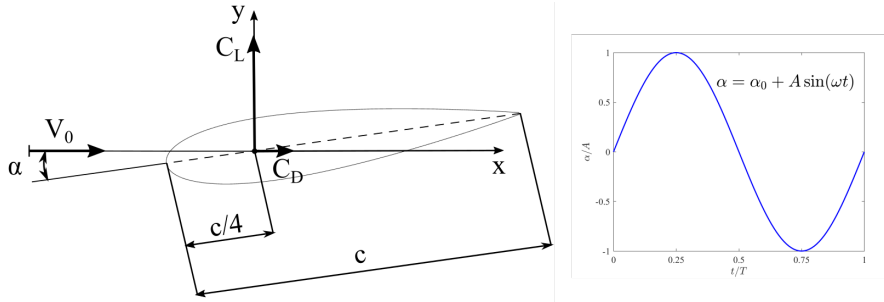


**Figure 1** Pitching NACA 0018 airfoil.

### 2.1 Simulation Setup and Turbulence Modeling

All numerical simulations summarized in this paper were conducted using the unsteady Reynolds-Averaged Navier-Stokes (URANS) approach. The computational domain was developed based on the working section of the Red Wind Tunnel (RWT) at TU Delft.

The wind tunnel's test section measures 2000 mm in length and 500 mm in height. Its width gradually increases from 750 mm at the inlet to 770 mm at the outlet. This slight expansion compensates for boundary layer growth along the walls and ensures an

almost zero pressure gradient in the empty tunnel. The turntable center is positioned 750 mm from the inlet. Additional details about the experimental setup and settings can be found in [28].

The URANS approach employed in these simulations required one of two methods: dynamic mesh or sliding mesh. The sliding mesh method, though less computationally demanding, necessitates defining an additional domain surrounding the oscillating foil. In our model, a circular domain with a diameter of two chord lengths was considered around the airfoil, with its center coinciding with the origin of the defined coordinate system [29].

The solver used was pressure-based and transient, with air as the working fluid. The air was modeled with constant density,  $\rho = 1.225 \text{ kg/m}^3$ , and constant viscosity,  $\mu = 1.7895 \times 10^{-5} \text{ kg/(ms)}$ . The boundary conditions were specified as follows: a velocity inlet at the left vertical edge of the domain, a pressure outlet at the right edge of the tunnel, and no-slip walls along both the tunnel walls and the airfoil surface [30].

As noted earlier, the sliding mesh approach was utilized in this study. This method required the creation of two regions: a stationary region and a moving region that oscillated with the airfoil. An interface was defined at the boundary between these two regions to facilitate their interaction.

For the numerical solution of the momentum equations and turbulence model equations, a second-order upwind discretization scheme was employed, along with a least-squares cell-based gradient evaluation. Pressure-velocity coupling was achieved using the SIMPLE algorithm. The residuals for all equations were maintained at a level of  $10^{-7}$ . In transient simulations, the maximum number of iterations per time step was set to 20. The time step size corresponded to an angular step size of  $0.5^\circ$ , which was sufficient to achieve satisfactory azimuthal resolution within the prescribed iteration limit per time step [30].

The present study focuses on the flow over a thick airfoil at low Reynolds numbers, where the formation of laminar separation bubbles plays a significant role in determining the aerodynamic characteristics. These bubbles can notably impact lift and drag, making their accurate prediction essential for understanding the flow behavior.

To accurately capture the complex flow phenomena associated with laminar separation bubbles, the Transition SST turbulence model, also known as the  $\gamma - Re_\theta$  model, is employed in this study. Developed by Langtry [15] and Menter et al. [31], this model builds upon the widely used  $k-\omega$  Shear Stress Transport (SST) framework by introducing two additional transport equations: one for the momentum-thickness Reynolds number,  $Re_\theta$ , and another for intermittency,  $\gamma$ . These enhancements enable the precise prediction of laminar-to-turbulent transition, which is crucial for flows influenced by separation bubbles.

Implemented in the ANSYS Fluent solver, the Transition SST model employs a correlation-based approach reliant on local flow variables, making it suitable for a wide range of engineering applications. By simultaneously resolving the turbulent kinetic energy, its dissipation rate, and transition-specific parameters, this model provides a more accurate representation of flow physics. Comprehensive details of the model's formulation can be found in the works of Langtry [15] and Menter et al [31].

In addition to the  $\gamma - Re_\theta$  approach, for comparison purposes, certain cases were also computed using the well-known two-equation  $k-\omega$  Shear Stress Transport (SST) turbulence model to highlight the differences between the two modeling approaches.

## 2.2 Numerical Mesh

The computational domain, shown in Fig. 2, was discretized using a hybrid mesh: a structured mesh near the airfoil edges and tunnel walls, and an unstructured mesh in the remaining regions. The application of a structured mesh is essential to accurately resolve the flow in the boundary layer near wall surfaces. The mesh on the airfoil surface consists of a total of 1669 nodes: 830 nodes along the upper edge, 830 along the lower edge, and 9 nodes at the trailing edge. A uniform element distribution was employed.

The structured mesh near the airfoil edges was constructed with 37 layers, with a growth rate of 1.13 in the direction normal to the surface. The thickness of the first wall-adjacent element was set to  $5 \times 10^{-6}$  m. This resolution was validated by the authors of this paper and adheres to the recommendations of ANSYS Fluent v2024. The thickness of the first element ensures that the wall  $y^+$  criterion ( $y^+ \leq 1.0$ ) is satisfied for all cases considered in this study.

At the interfaces, a uniform element size of  $5 \times 10^{-4}$  m was used. For the tunnel walls, a structured mesh was applied with the following parameters: the thickness of the first element was  $5 \times 10^{-6}$  m, 40 layers in the normal direction, and an element growth rate of 1.2. Similar to the structured mesh around the airfoil edges, these parameters are consistent with ANSYS Fluent guidelines and meet the wall  $y^+$  criterion [30].

In the unstructured mesh, the moving domain surrounding the airfoil employed elements with a size of  $5 \times 10^{-4}$  m. In the stationary domain, the element size was  $4 \times 10^{-3}$  m. Additionally, a smaller region within the stationary domain, extending 1 chord length ( $1c$ ) from the interface to the outlet edge of the tunnel, was defined. This modification was made to better resolve the flow in the wake region. In this additional region, the element size was  $2 \times 10^{-3}$  m. The chosen element sizes are sufficient even for LES simulations [32], [33].

The nominal mesh designed in this manner comprises a total of 285,016 nodes and 282,934 elements.

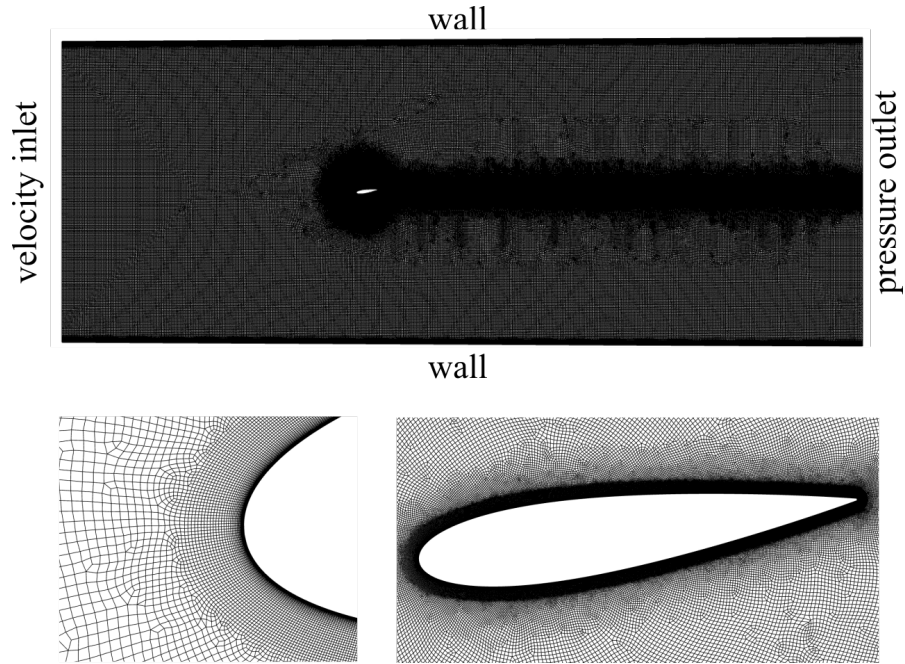


**Figure 2** Numerical mesh: entire domain (top image) and zoomed-in mesh around the airfoil (bottom images). Additionally, boundary conditions are depicted in the top image.

A mesh sensitivity analysis was conducted to evaluate the influence of grid resolution on the numerical solution. This test was performed for a stationary case, where the frequency of the pitching motion of the NACA 0018 airfoil was set to zero.

The analysis was carried out at a fixed angle of attack of  $8^\circ$  and at the highest Reynolds number considered in this study,  $Re = 160,000$ . Four different meshes were used: two coarser meshes with the number of nodes reduced by factors of  $\sqrt{2}$  and 2 compared to the nominal mesh, and one finer mesh with the number of nodes on the airfoil surface increased by a factor of  $\sqrt{2}$  relative to the nominal configuration.

The lift and drag coefficients as functions of the number of nodes on the airfoil surface are presented in Fig. 3. The results clearly indicate that the lift coefficient is independent of the grid resolution, while the drag coefficient exhibits minimal sensitivity to the number of nodes. In other words, increasing the number of nodes beyond the nominal mesh resolution does not enhance the accuracy of the computed aerodynamic loads but merely raises the computational cost.

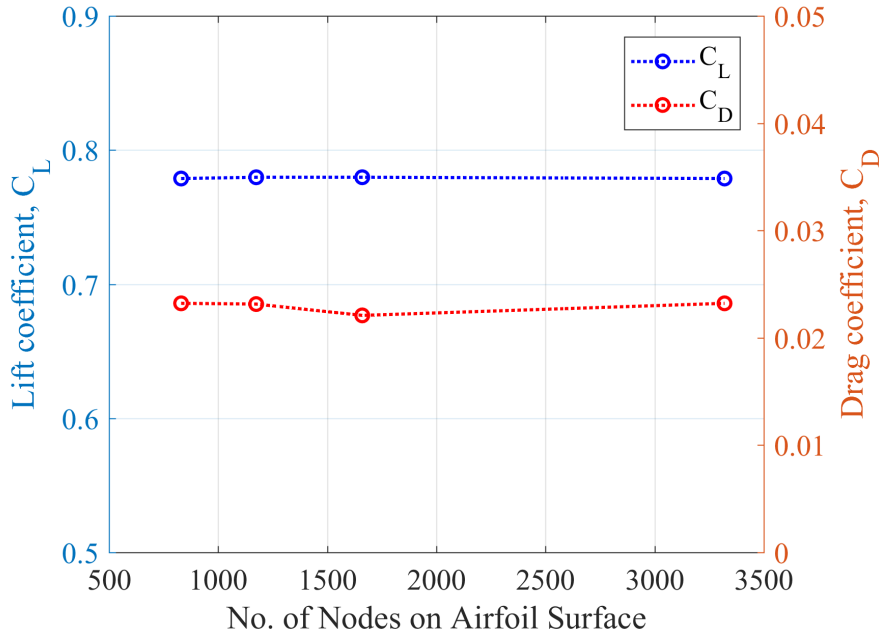


**Figure 3** Mesh sensitivity analysis: Lift coefficient ( $C_L$ ) and drag coefficient ( $C_D$ ) as functions of the number of nodes on the airfoil surface. The results indicate that  $C_L$  is independent of the grid resolution, while  $C_D$  exhibits minimal sensitivity to the number of nodes. Increasing the grid resolution beyond the nominal mesh does not significantly enhance accuracy but increases computational cost.

The flow simulations around the NACA 0018 airfoil, even for the "no pitch" case and at low angles of attack, required the use of the unsteady Reynolds-averaged Navier-Stokes (URANS) approach with the advanced  $\gamma - Re_\theta$  transition model. This was due to the high temporal variability of the physical phenomena occurring within the boundary layer near the airfoil's surface. The application of the URANS approach necessitates the definition of a time step [11].

In this work, the SIMPLE (Semi-Implicit Method for Pressure-Linked Equations) algorithm was utilized. In SIMPLE, there is no need to set the Courant-Friedrichs-Lewy (CFL) condition because SIMPLE is an iterative method that is not directly dependent on the time step size. Instead, SIMPLE operates based on quasi-static computations, where the pressure and velocity equations are solved iteratively until convergence is achieved. As a result, the stability of the solution is not directly affected by the time step size or the CFL number. This makes the SIMPLE method "unconditionally stable" in a numerical sense [30].

The time step applied for the "no pitch" case was 0.001 seconds. For cases where the pitch motion was greater than zero, the time step was set to 1/720 of the period. Specifically, for a frequency of 1 Hz, the time step was 0.001388 seconds, whereas for a frequency of 2 Hz, it was 0.0006944 seconds.

## 3 Aerodynamic Load Analysis for the Pitching NACA 0018 Airfoil

### 3.1 Aerodynamic Load Analysis for 0 Hz Pitching Motion

Figure 4 presents the aerodynamic characteristics,  $C_L$  and  $C_D$ , as functions of the angle of attack,  $\alpha$ , for the NACA 0018 airfoil. The analysis was conducted for two Reynolds numbers,  $Re = 80k$  and  $Re = 160k$ . Numerical simulations were performed over an angle of attack range from  $0^\circ$  to  $20^\circ$  to capture the stall point. Although the results represent steady aerodynamic characteristics, they were obtained using the URANS approach and averaged over the last second of simulation.

The primary turbulence model used in this study was the four-equation  $\gamma - Re_\theta$  transition model. For comparison, the two-equation  $k-\omega$  SST turbulence model was also employed. Additionally, experimental data obtained by the authors in the low-turbulence wind tunnel at the Technical University of Denmark were included. The experimental results, along with data from the well-known XFOIL tool, were summarized in Rogowski et al [28].

The figure highlights a strong sensitivity of aerodynamic forces to the Reynolds number. Notably, the experimental lift coefficient ( $C_L$ ) exhibits nonlinear behavior below the critical angle of attack. As proposed by Rogowski et al., this nonlinearity arises from the presence and evolution of laminar separation bubbles. These bubbles increase lift at low angles of attack but also significantly raise drag. A decrease in Reynolds number by half reduces  $C_{L_{\max}}$  from 1.027 at  $\alpha = 13.99^\circ$  to 0.803 at  $\alpha = 7.95^\circ$ . Interestingly, at  $\alpha = 3.96^\circ$ , the lift coefficient is higher for the lower Reynolds number, with values of 0.406 for  $Re = 160k$  and 0.578 for  $Re = 80k$ .

These physical phenomena are challenging to model numerically. The least accurate results were obtained with the fully turbulent  $k-\omega$  SST model, which produces linear lift characteristics up to the critical angle. However, at  $Re = 160k$  and low angles of attack (up to  $3^\circ-4^\circ$ ) as well as near the critical angle ( $12^\circ-14^\circ$ ), the discrepancies in lift and drag are less significant. Despite overestimating drag coefficients at  $Re = 160k$ , the drag coefficient for the SST model converges more closely to experimental values at lower Reynolds numbers, with a deviation of only 15.6% at  $Re = 80k$ . This can be attributed to increased boundary layer interactions at lower Reynolds numbers, leading to higher form drag.

XFOIL demonstrates a similar trend for lift, with higher coefficients at lower angles of attack for lower Reynolds numbers. However,  $C_{L_{\max}}$  predicted by XFOIL is overestimated compared to experimental results across the entire angle of attack range. This overprediction may stem from the lack of calibration of XFOIL for thick airfoils, as the model was initially developed for flat plates. Additionally, this study did not examine the effect of the transition parameter  $N$ , which was set to the default value of 9. While appropriate for low-turbulence wind tunnels, even slight changes in turbulence intensity at low Reynolds numbers can significantly affect aerodynamic characteristics. Interestingly, XFOIL predicts a minimum drag coefficient at a nonzero angle of attack, with drag decreasing slightly (by about 8%) as  $\alpha$  increases from  $0^\circ$  to  $4^\circ$  at  $Re = 80k$ .

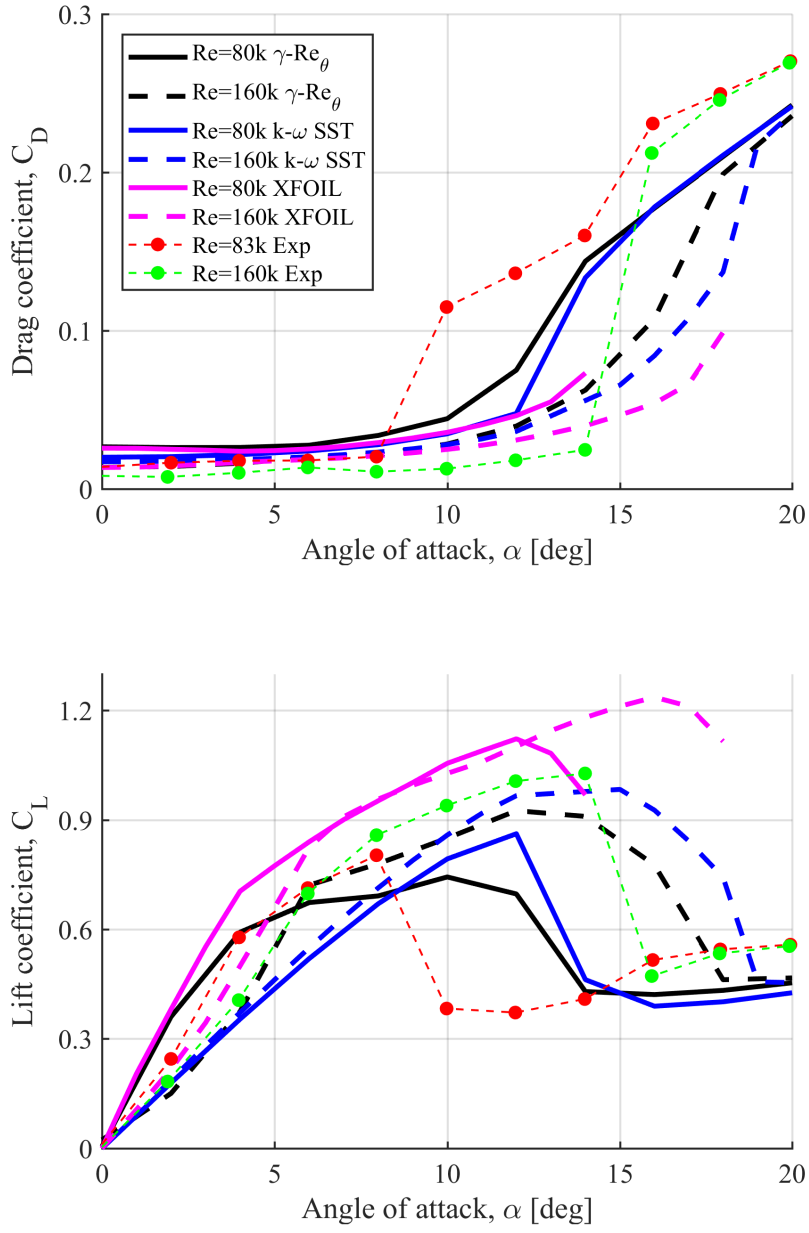


**Figure 4** Comparison of drag coefficient ( $C_D$ , top subplot) and lift coefficient ( $C_L$ , bottom subplot) as functions of the angle of attack,  $\alpha$ , for different Reynolds numbers ( $Re = 80k$  and  $Re = 160k$ ) and modeling approaches. Experimental data from [28].

As mentioned in Section 2.2, when analyzing the flow around a clean airfoil under low Reynolds number conditions, even in the "no pitch" scenario, a transient approach must be considered due to the unsteady phenomena occurring within the boundary layer.

As discussed in the Introduction, the magnitude and frequency of these unsteady phenomena depend on the Reynolds number and angle of attack. In practice, the magnitude of these unsteady effects manifests as oscillations in aerodynamic forces, both in their amplitude and frequency. As shown in Fig. 5, the largest oscillations in the lift coefficient ( $C_L$ ) are observed for a Reynolds number of 160k, particularly at angles of attack up to  $8^\circ$ . These oscillations decrease around the stall angle but begin to grow again at higher angles of attack. A similar behavior is observed for the drag coefficient ( $C_D$ ), although its oscillation amplitudes are significantly smaller. In contrast, for a Reynolds number of 80k, the oscillations in aerodynamic forces are much smaller. The aerodynamic characteristics  $C_L$  and  $C_D$  shown in Fig. 4 represent the time-averaged values of  $C_L(\text{time})$  and  $C_D(\text{time})$  (Fig. 5) over the last second of simulation.

Figure 6 compares the pressure coefficient ( $C_p$ ) and  $x$ -wall shear stress distributions along the chordwise coordinate ( $x/c$ ) for the two examined Reynolds numbers and three representative angles of attack ( $2^\circ$ ,  $4^\circ$ , and  $8^\circ$ ). These plots confirm that for a Reynolds number of 160k, the intensity of the laminar separation bubbles is significantly higher compared to  $Re = 80k$ . Furthermore, at lower angles of attack, the bubbles shift closer to the airfoil leading edge.

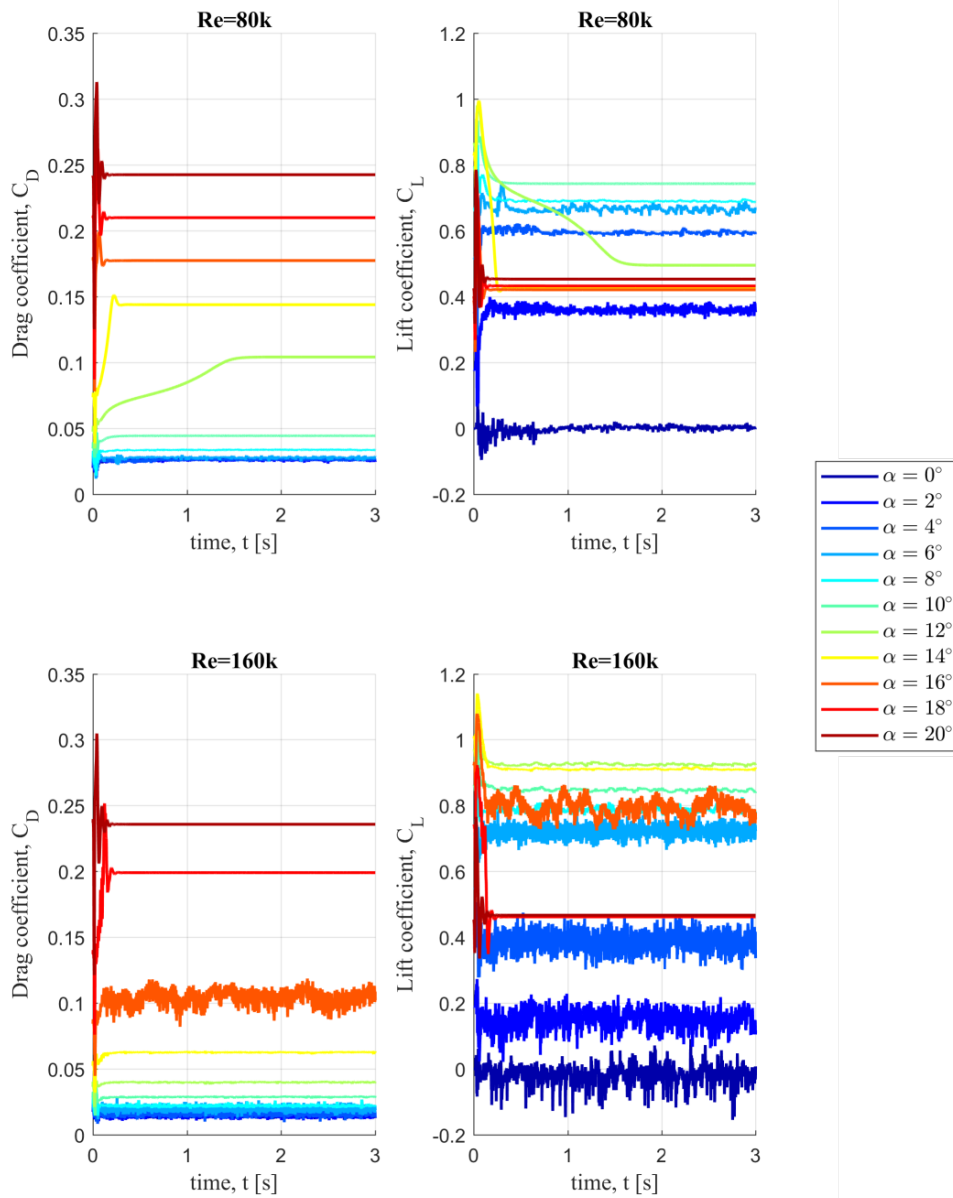


**Figure 5** Comparison of drag ( $C_D$ ) and lift ( $C_L$ ) coefficients over time for different angles of attack ( $\alpha$ ) at Reynolds numbers of 80k (top row) and 160k (bottom row). The left column shows  $C_D$ , while the right column presents  $C_L$ .

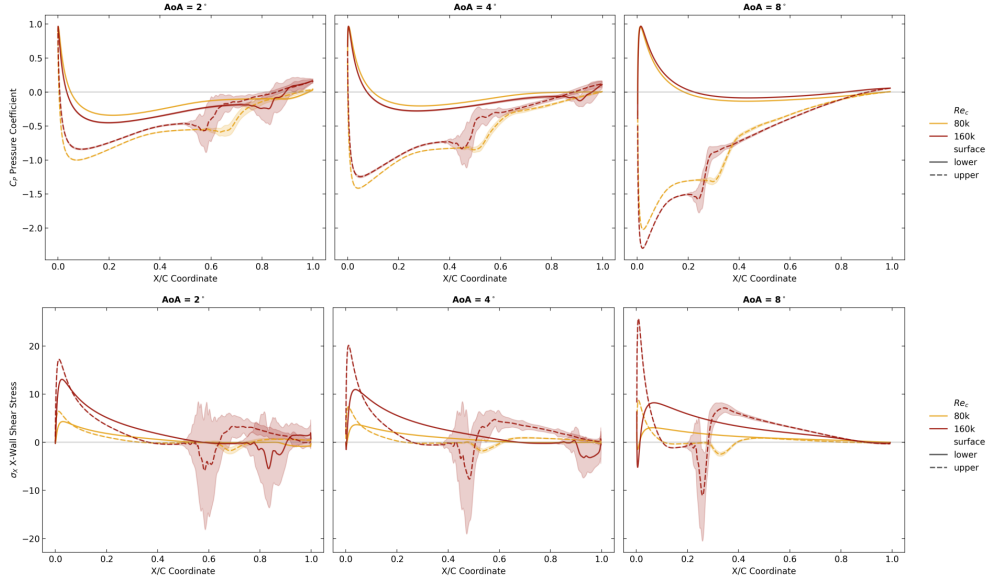


**Figure 6** Comparison of pressure coefficient ( $C_p$ ) and wall shear stress ( $\tau_x$ ) distributions along the airfoil chord ( $X/C$ ) at different angles of attack ( $2^\circ$ ,  $4^\circ$ , and  $8^\circ$ ) for Reynolds numbers of 80k and 160k. The top row presents  $C_p$  distributions, while the bottom row shows  $\sigma_x$ . Solid lines correspond to the lower surface, and dashed lines to the upper surface.

### 3.2 Aerodynamic Load Analysis for 1 Hz Pitching Motion

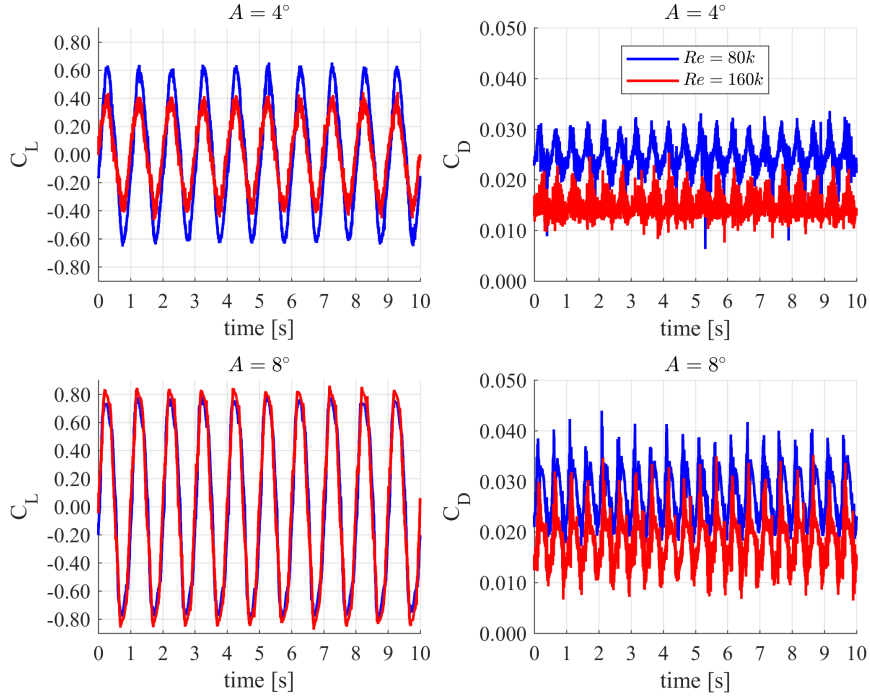
This section presents the results of the aerodynamic load analysis for the pitching NACA 0018 airfoil. The study investigates the influence of the Reynolds number on aerodynamic force coefficients, considering two pitching amplitudes:  $4^\circ$  and  $8^\circ$ . The frequency of the 1 Hz pitching motion corresponds to a reduced frequency of approximately 0.01 for  $Re = 80k$  and around 0.005 for  $Re = 160k$ , highlighting the influence of the Reynolds number on the normalized temporal scaling of the motion.

It was observed that the drag coefficient component is the most sensitive to both the Reynolds number and the amplitude of pitching (Figure 7). To confirm the influence of the Reynolds number on the drag coefficient, its values were averaged over the last computed cycle of motion.

For the amplitude  $A = 4^\circ$ , the drag coefficient for  $Re = 80k$  is approximately 67% higher compared to  $Re = 160k$ . For  $A = 8^\circ$ , the drag coefficient is about 51% higher under the same comparison.

Our observations further revealed that the maximum values of the lift coefficient for the amplitude  $A = 4^\circ$  are higher for the lower Reynolds number. The maximum drag coefficient in this case is about 44% higher compared to  $Re = 160k$  at the same amplitude. Interestingly, for the amplitude  $A = 8^\circ$ , the opposite is true - the lift maxima for  $Re = 160k$  are greater, though the difference in these maxima is significantly smaller.

For both analyzed amplitudes and Reynolds numbers under investigation, the mean values of the normal force coefficient are, as expected, very close to zero.



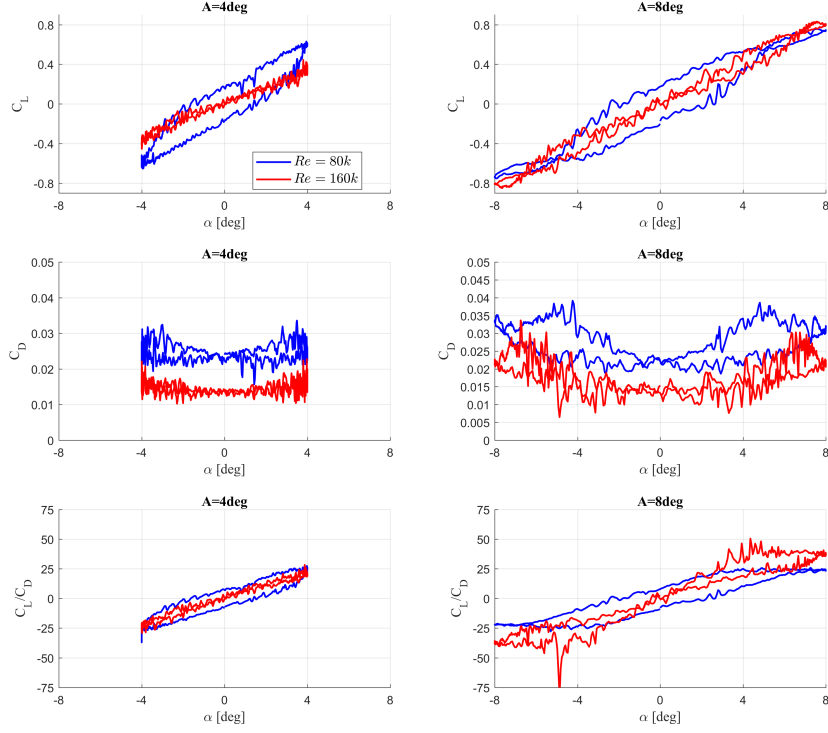
**Figure 7** Time histories of the lift coefficient ( $C_L$ ) and drag coefficient ( $C_D$ ) for pitching amplitudes  $A = 4^\circ$  and  $A = 8^\circ$  at Reynolds numbers  $Re = 80k$  and  $Re = 160k$ . The top row corresponds to  $A = 4^\circ$ , while the bottom row corresponds to  $A = 8^\circ$ .

Figure 7 illustrates the influence of the Reynolds number on aerodynamic loads as a function of time. For better comparison, the same results for the aerodynamic force coefficients are also presented in a different format, plotted against the angle of attack  $\alpha$ . Figure 8 shows the comparison of the hysteresis loops of the aerodynamic force coefficients under the investigated wing motion parameters. In the case of the lift coefficient, the hysteresis loop is widest around the angle of attack  $\alpha = 0^\circ$ . An increase in the Reynolds number from 80k to 160k reduces the loop width for both the lift and drag coefficients.

The top-left panel of Figure 8 highlights the significant impact of the Reynolds number on the shape and slope of the lift coefficient as a function of the angle of attack. Furthermore, Figure 8 compares the relationship between the lift-to-drag ratio ( $C_L/C_D$ ) and the angle of attack for two Reynolds numbers, 80k and 160k.

This comparison reveals a considerably smaller influence of the Reynolds number on the aerodynamic efficiency, particularly for the smaller amplitude of  $4^\circ$ . This indicates that the higher drag associated with the lower Reynolds number offsets the potential benefits of the higher lift coefficient values.

For the larger amplitude under investigation, a higher Reynolds number results in greater values of the  $C_L/C_D$  ratio, especially at higher angles of attack.



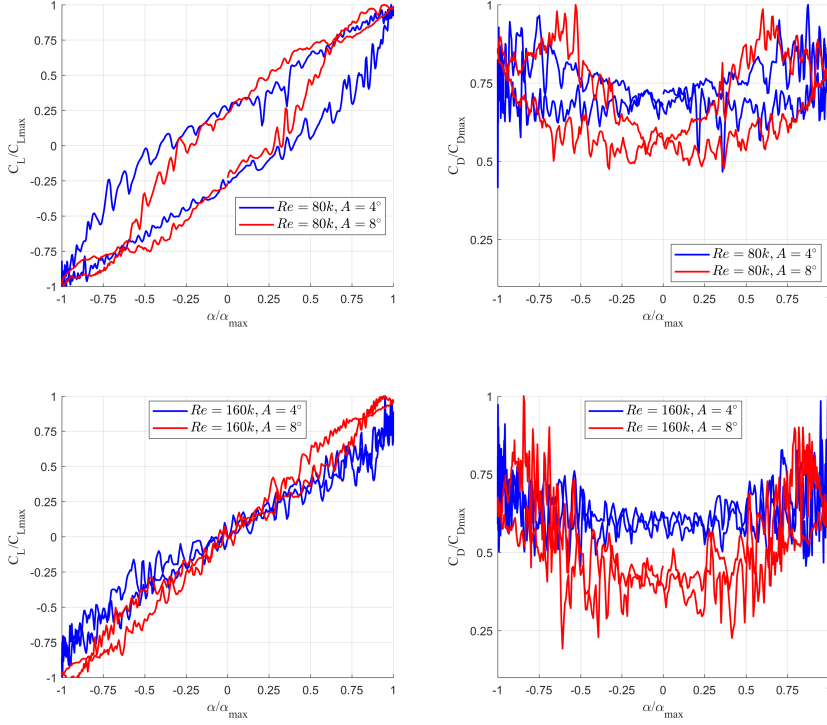
**Figure 8** Hysteresis loops of the lift coefficient ( $C_L$ ), drag coefficient ( $C_D$ ), and lift-to-drag ratio ( $C_L/C_D$ ) as a function of the angle of attack ( $\alpha$ ) for pitching amplitudes  $A = 4^\circ$  and  $A = 8^\circ$  at Reynolds numbers  $Re = 80k$  and  $Re = 160k$ . The left column corresponds to  $A = 4^\circ$ , and the right column corresponds to  $A = 8^\circ$ .

Figure 9 was created to illustrate the influence of the amplitude on hysteresis loops at a given Reynolds number. To compare the aerodynamic force coefficients for different amplitudes, the values of the coefficients were normalized by their respective maximum values. A similar normalization was applied to the angles of attack.

The plots presented in this figure reveal that the amplitude has the greatest impact on the drag coefficient at low angles of attack. For both Reynolds numbers, the

minimum drag coefficient for the amplitude  $A = 8^\circ$  was lower compared to  $A = 4^\circ$ . This is most likely associated with the higher linear velocity of the leading edge.

As shown in the top-left panel, the Reynolds number also significantly affects the lift coefficient. The largest differences are observed for  $\alpha/\alpha_{\max}$  in the range from 0.5 to 1.0.



**Figure 9** Normalized lift coefficient ( $C_L/C_{L,\max}$ ) and drag coefficient ( $C_D/C_{D,\max}$ ) as a function of normalized angle of attack ( $\alpha/\alpha_{\max}$ ) for Reynolds numbers  $Re = 80k$  and  $Re = 160k$ , and pitching amplitudes  $A = 4^\circ$  and  $A = 8^\circ$ . The top row compares  $Re = 80k$ , while the bottom row compares  $Re = 160k$ .

### 3.3 Aerodynamic Forces Predicted by the $k-\omega$ SST Model for Pitching Motion

This section presents the dynamic characteristics of the harmonically oscillating NACA0018 airfoil using the classical 2-equation  $k-\omega$  SST turbulence model. Figure 10 compares the aerodynamic force components in the time domain.

The aerodynamic forces generated on the surface of the oscillating airfoil are, as expected, nearly harmonic functions. Due to the wall-layer modeling approach, no

irregularities associated with laminar separation bubbles are visible in the characteristics. In contrast to the  $\gamma - Re_\theta$  model, the  $k-\omega$  SST turbulence model shows that the maximum lift coefficient values calculated for the case  $A = 4^\circ$  and  $Re = 160,000$  are slightly higher compared to  $Re = 80,000$ .

An increase in amplitude to  $8^\circ$  results in a slight increase in the difference between amplitudes. Despite minor differences in lift force estimation, drag is much more dependent on the Reynolds number, as shown in the right-hand column of the plots in Figure 10.

The drag coefficient at the lower amplitude ( $A = 4^\circ$ ) exhibits an almost entirely periodic nature, repeating in each cycle of airfoil oscillation. This indicates the establishment of a steady dynamic regime where the aerodynamic response is cyclically repeatable.

For the oscillation amplitude of  $8^\circ$  and Reynolds number  $Re = 80,000$ , very small differences in successive drag force amplitudes were observed. This may result from the proximity to the critical static angle of attack, which affects the flow characteristics around the airfoil and stabilizes the aerodynamic forces.

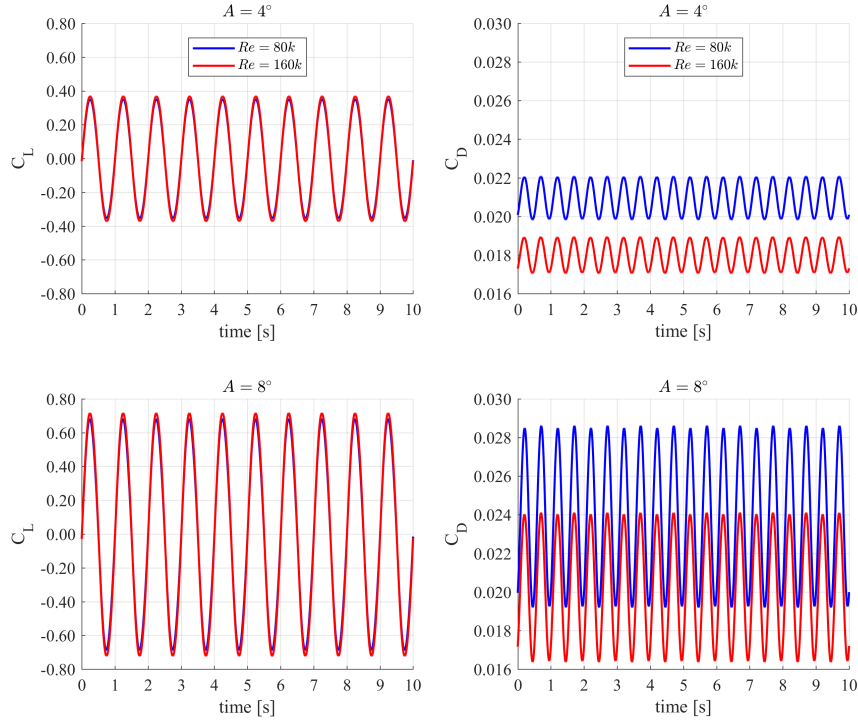


**Figure 10** Time histories of the lift coefficient ( $C_L$ ) and drag coefficient ( $C_D$ ) for pitching amplitudes  $A = 4^\circ$  and  $A = 8^\circ$  at Reynolds numbers  $Re = 80k$  and  $Re = 160k$ . The top row corresponds to  $A = 4^\circ$ , while the bottom row corresponds to  $A = 8^\circ$ .

The characteristics of aerodynamic force coefficients and aerodynamic efficiency as a function of the angle of attack are shown in Figure 11. All plots reveal the absence of effects associated with laminar separation bubbles.

The hysteresis loops of  $C_L$  are nearly identical for  $A = 4^\circ$  and  $A = 8^\circ$ , showing only a scaling effect. For the  $C_D$  hysteresis, a practically uniform shift dependent only on the Reynolds number is visible. The characteristics are symmetrical about  $\alpha = 0^\circ$ .

Additionally, the Reynolds number is reflected in the slightly different slopes of the  $C_L/C_D$  ratio. This highlights the role of Reynolds number in determining aerodynamic efficiency under dynamic conditions.

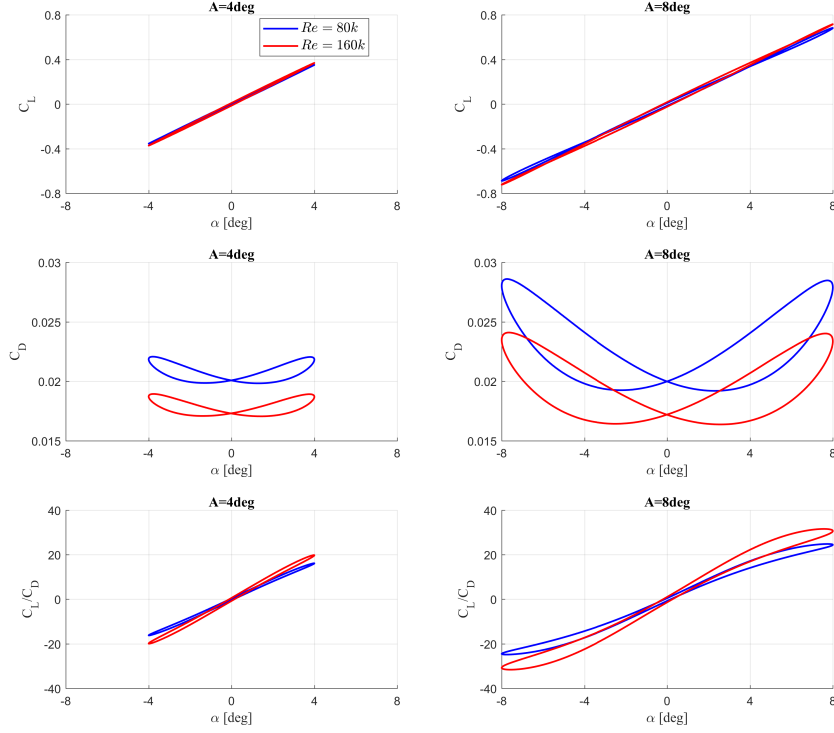


**Figure 11** Hysteresis loops of the lift coefficient ( $C_L$ ), drag coefficient ( $C_D$ ), and lift-to-drag ratio ( $C_L/C_D$ ) as a function of the angle of attack ( $\alpha$ ) for pitching amplitudes  $A = 4^\circ$  and  $A = 8^\circ$  at Reynolds numbers  $Re = 80k$  and  $Re = 160k$ . The left column corresponds to  $A = 4^\circ$ , and the right column corresponds to  $A = 8^\circ$ .

Figure 12 illustrates the greater influence of the Reynolds number on the ratio  $C_L/C_{Lmax}$  as a function of the normalized angle of attack. An increase in  $Re$  causes a broader hysteresis for small angles of attack.

Interestingly, the shape of the  $C_L/C_{L,max}$  curve depends more on the Reynolds number than on the amplitude. Similarly, the Reynolds number has a more significant impact on the drag coefficient, although in this case, amplitude plays a key role.

As with the turbulence model accounting for laminar-to-turbulent transition, a significant drop in  $\alpha/\alpha_{max}$  is observed for the higher amplitude case.

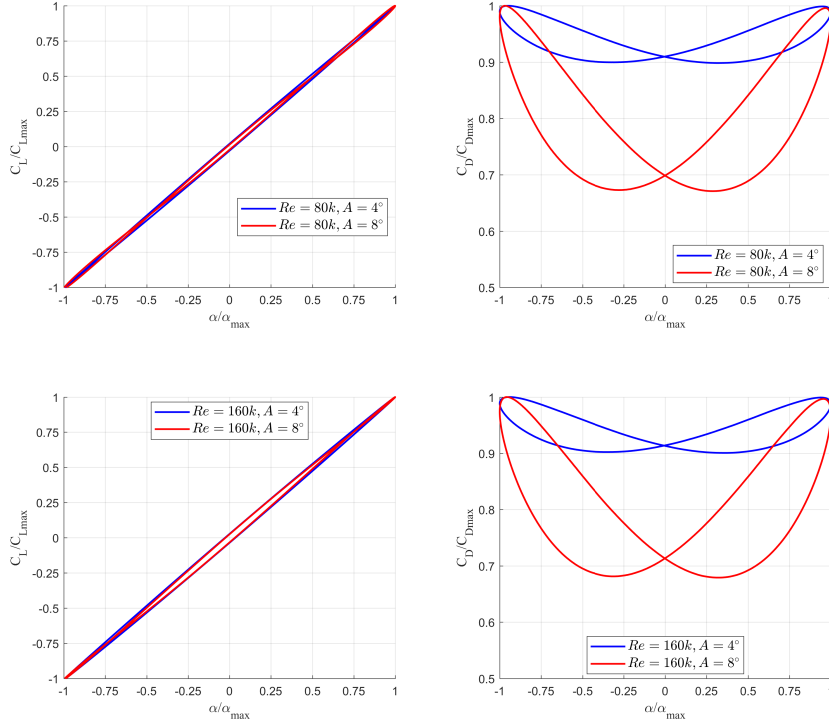


**Figure 12** Normalized lift coefficient ( $C_L/C_{L,max}$ ) and drag coefficient ( $C_D/C_{D,max}$ ) as a function of normalized angle of attack ( $\alpha/\alpha_{max}$ ) for Reynolds numbers  $Re = 80k$  and  $Re = 160k$ , and pitching amplitudes  $A = 4^\circ$  and  $A = 8^\circ$ . The top row compares  $Re = 80k$ , while the bottom row compares  $Re = 160k$ .

### 3.4 Aerodynamic Load Analysis for 2 Hz Pitching Motion

The reduced frequencies for the 2 Hz pitching motion are approximately 0.02 for  $Re = 80k$  and 0.01 for  $Re = 160k$ . The time histories of the aerodynamic force coefficients, shown in Fig. 13, exhibit a similar qualitative trend as observed for the 1 Hz pitching motion.

For the lower Reynolds number of  $Re = 80k$ , the maximum values of  $C_L$  are higher compared to those for  $Re = 160k$ . However, for the amplitude  $A = 8^\circ$ , the differences

in maximum  $C_L$  values between the two Reynolds numbers are significantly smaller, similar to the 1 Hz case.

Both the Reynolds number and the amplitude primarily influence the drag coefficient, which is consistently lower for the higher Reynolds number.

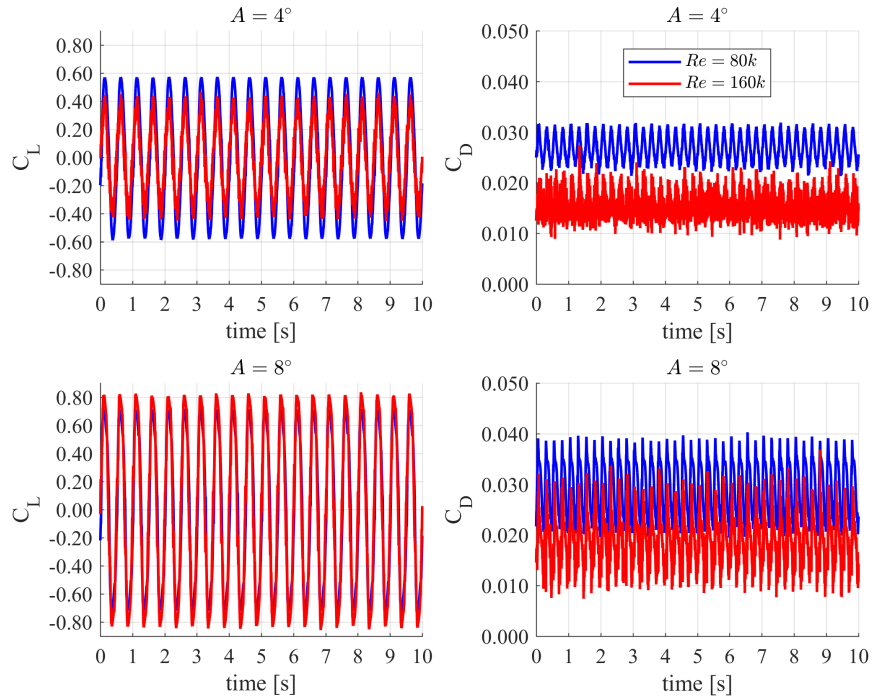


**Figure 13** Time histories of the lift coefficient ( $C_L$ ) and drag coefficient ( $C_D$ ) for pitching amplitudes  $A = 4^\circ$  and  $A = 8^\circ$  at Reynolds numbers  $Re = 80k$  and  $Re = 160k$ . The top row corresponds to  $A = 4^\circ$ , while the bottom row corresponds to  $A = 8^\circ$ .

An interesting observation, as seen in Fig. 13 and even more clearly in Fig. 14, which depicts the aerodynamic force coefficients as a function of the angle of attack, is the less oscillatory nature of the coefficients for the Reynolds number  $Re = 80k$ . For  $Re = 160k$ , oscillations are more pronounced but remain smaller compared to the 1 Hz case.

The remaining qualitative effects for both Reynolds numbers, including the aerodynamic force coefficients and the lift-to-drag ratio ( $C_L/C_D$ ), are consistent with the trends discussed in Subsection 3.2 of this paper.

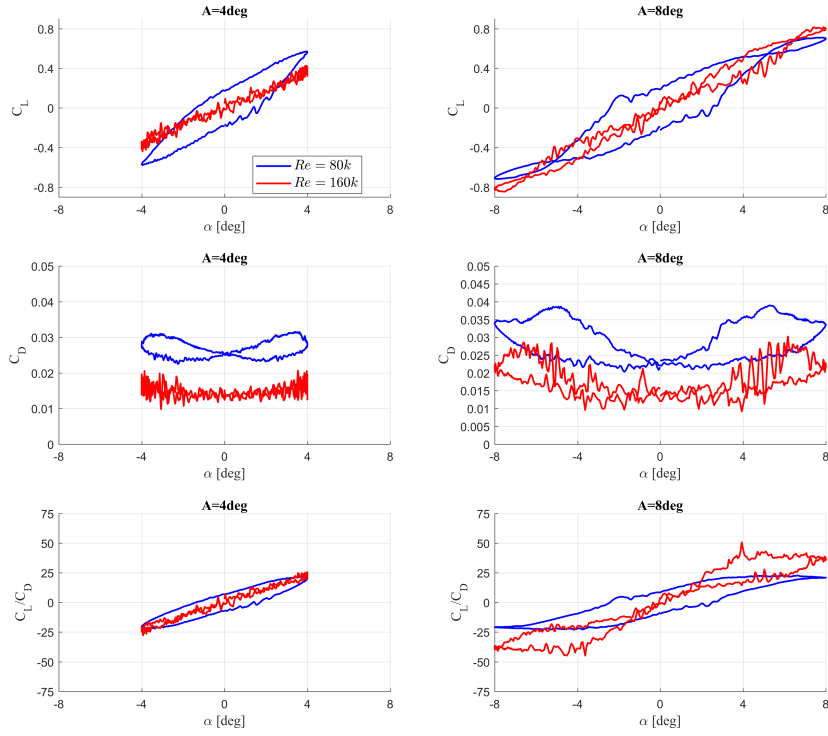


**Figure 14** Hysteresis loops of the lift coefficient ( $C_L$ ), drag coefficient ( $C_D$ ), and lift-to-drag ratio ( $C_L/C_D$ ) as a function of the angle of attack ( $\alpha$ ) for pitching amplitudes  $A = 4^\circ$  and  $A = 8^\circ$  at Reynolds numbers  $Re = 80k$  and  $Re = 160k$ . The left column corresponds to  $A = 4^\circ$ , and the right column corresponds to  $A = 8^\circ$ .

Figure 15 compares the normalized lift and drag coefficients as a function of the normalized angle of attack. This comparison clearly shows that, for the Reynolds number of  $Re = 80k$ , the effect of laminar separation bubbles is significantly smaller than for  $Re = 160k$ . Similar to the 1 Hz frequency case, a notable reduction in the minimum drag coefficient is observed for the higher amplitude.

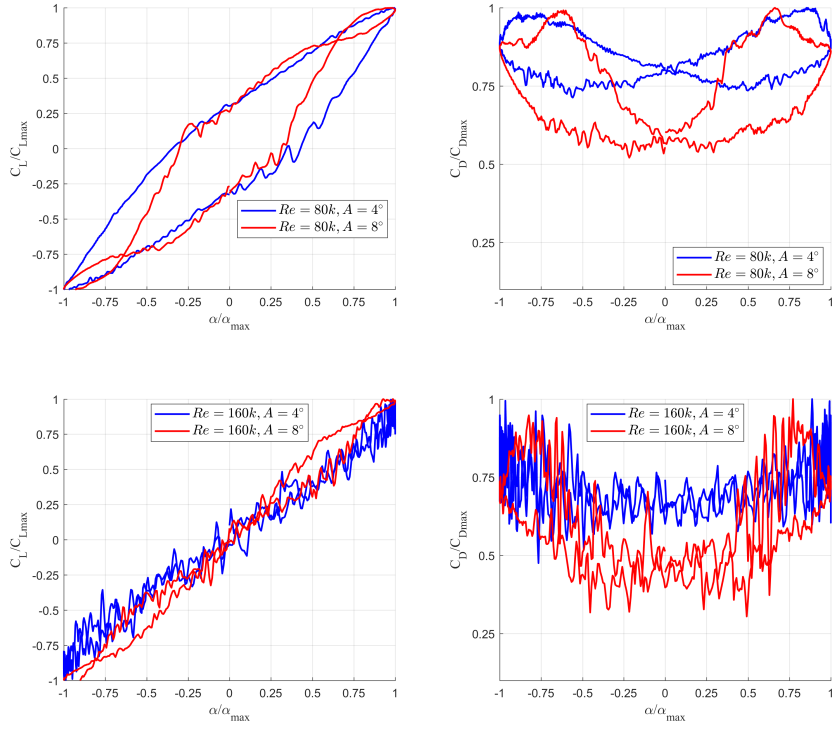


**Figure 15** Normalized lift coefficient ( $C_L/C_{L,\max}$ ) and drag coefficient ( $C_D/C_{D,\max}$ ) as a function of normalized angle of attack ( $\alpha/\alpha_{\max}$ ) for Reynolds numbers  $Re = 80k$  and  $Re = 160k$ , and pitching amplitudes  $A = 4^\circ$  and  $A = 8^\circ$ . The top row compares  $Re = 80k$ , while the bottom row compares  $Re = 160k$ .

### 3.5 Hysteresis Loop Analysis for the Pitching Airfoil

In Section 3.4, the aerodynamic load characteristics, including the lift and drag components on the surface of the pitching airfoil, were analyzed as a function of the Reynolds number and amplitude. Both factors significantly influence the behavior of the characteristics and the shape of the hysteresis loop.

The wide loop observed at low angles of attack is primarily attributed to phenomena occurring in the boundary layer, particularly the detachment of the laminar boundary layer. Figure 16 illustrates the detachment location as a function of the dimensionless time  $t/T$ , where  $t$  is the time and  $T$  is the motion period.

This figure shows the evolution of the pressure coefficient ( $C_p$ ) and x-wall shear stress for a pitch angle varying from 0 to its maximum value. The analysis considers an amplitude  $A = 4^\circ$  and  $Re = 80k$ . Based on the x-wall shear stress characteristics,

the local position of the laminar boundary layer separation can be identified, which is marked by a change in the x-wall shear stress from positive to negative.

On the  $C_p$  plots, the separation is reflected by a stagnation region (a flat part of the curve). Figure 16c depicts the "migration" of the transition location,  $x_{tr}/c$ , normalized by the airfoil chord  $c$ . Different colors are used to represent the transition characteristics for the suction and pressure sides of the airfoil.

The figure demonstrates that as the pitch angle increases, the separation occurs later on the suction side and earlier on the pressure side. The contour map of the vorticity vector parallel to the z-axis, shown in Figure 16b, visualizes the aerodynamic wake surrounding the airfoil.

Both panels illustrate the same pitch angle of  $2^\circ$  during the increasing pitch angle (upper plot) and decreasing pitch angle (lower plot). The figure clearly reveals large vortex structures generated at the trailing edge on both sides of the airfoil. It also highlights their dependence on the direction of the airfoil's motion. Additionally, a slight curvature of the wake is observed during the decreasing pitch angle phase.

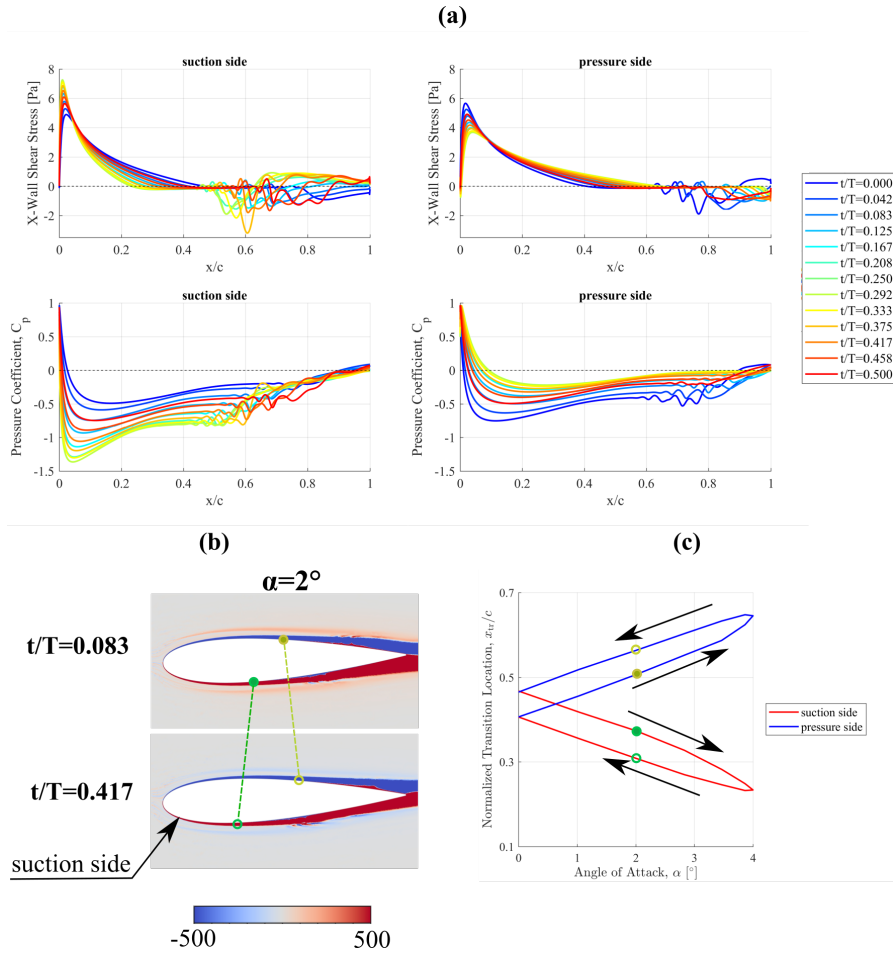


**Figure 16** Normalized lift coefficient ( $C_L/C_{L,max}$ ) and drag coefficient ((a) Pressure coefficient,  $C_p$ , and x-wall shear stresses; (b) z-vorticity contours; (c) normalized transition location,  $x_{tr}/c$ ).

### 3.6 Aerodynamic Load Analysis for 13 Hz Pitching Motion

This section discusses the case where the pitching motion frequency is 13.3(3) Hz. The reduced frequencies are 0.129 for  $Re = 80k$  and 0.065 for  $Re = 160k$ . The reason for analyzing the aerodynamic loads of a pitching NACA 0018 foil at this "unusual" frequency lies in the rotational speed of a Darrieus vertical-axis wind turbine (VAWT). This rotor was tested in the TU Delft wind tunnel, and the results of these tests can be found, among others, in [6]. Since the publication of these tests, numerous scientific papers have been devoted to this rotor.

Some authors naturally utilized the experimental data of this turbine to validate numerical methods, including the  $\gamma - Re_\theta$  transition model. Additionally, studies comparing the turbine's performance using various turbulence models, such as the  $k - \omega$  SST model, have emerged. Results published by various authors confirm that both

models generate similar results for aerodynamic loads, namely the tangential and normal components, as shown, for example, in [10], [34], and [35]. These minor discrepancies posed a puzzle since both models exhibit significant differences in the stationary lift force characteristics. Furthermore, as sections of this article discussing the force dynamics for a foil oscillating at 1 Hz and 2 Hz have shown, laminar separation bubbles play a substantial role in the oscillations of aerodynamic forces. Consequently, the lack of significant differences between the aerodynamic load characteristics obtained using the  $\gamma - Re_\theta$  transition model and the  $k - \omega$  SST model was partially attributed to turbulence intensity. As is known, the effect of bubbles diminishes with increasing turbulence intensity [36]. However, in the case of this particular rotor, this does not appear to be the main reason, as it was tested in a low-turbulence intensity wind tunnel [6].

The results presented in this section partially resolve the puzzle of the significant similarities in loads obtained using both approaches— $\gamma - Re_\theta$  and  $k - \omega$  SST. Figures 17 and 18 illustrate the hysteresis loops of aerodynamic coefficients at two examined Reynolds numbers and two amplitudes. Both figures compare the results of the two turbulence models, with dashed lines representing the  $k - \omega$  SST approach. As can be seen, the  $k - \omega$  SST model's results improve with increasing Reynolds number. Interestingly, the hysteresis of the  $C_L$  coefficient obtained using this model is broader for  $Re = 160k$  and  $A = 8^\circ$ , whereas the agreement between the two approaches for  $A = 4^\circ$  is very high. Additionally, the drag coefficients for both amplitudes at high Reynolds numbers are surprisingly consistent.

Another critical observation from these figures is the absence of aerodynamic load oscillations obtained using the  $\gamma - Re_\theta$  transition model, indicating a reduced impact of laminar separation bubbles. Comparing the results shown in this section with those in Section 3.4 further reveals that at lower oscillation frequencies, the bubble effect weakens in the case of lower Reynolds numbers.

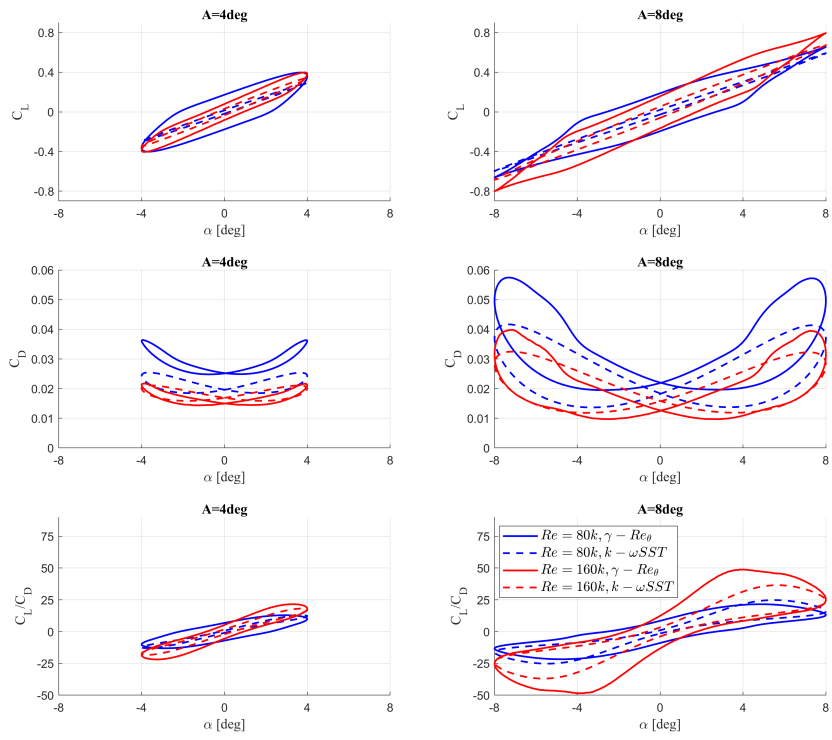


**Figure 17** Hysteresis loops of the lift coefficient ( $C_L$ ), drag coefficient ( $C_D$ ), and lift-to-drag ratio ( $C_L/C_D$ ) as a function of the angle of attack ( $\alpha$ ) for pitching amplitudes  $A = 4^\circ$  and  $A = 8^\circ$  at Reynolds numbers  $Re = 80k$  and  $Re = 160k$ . The left column corresponds to  $A = 4^\circ$ , and the right column corresponds to  $A = 8^\circ$ .

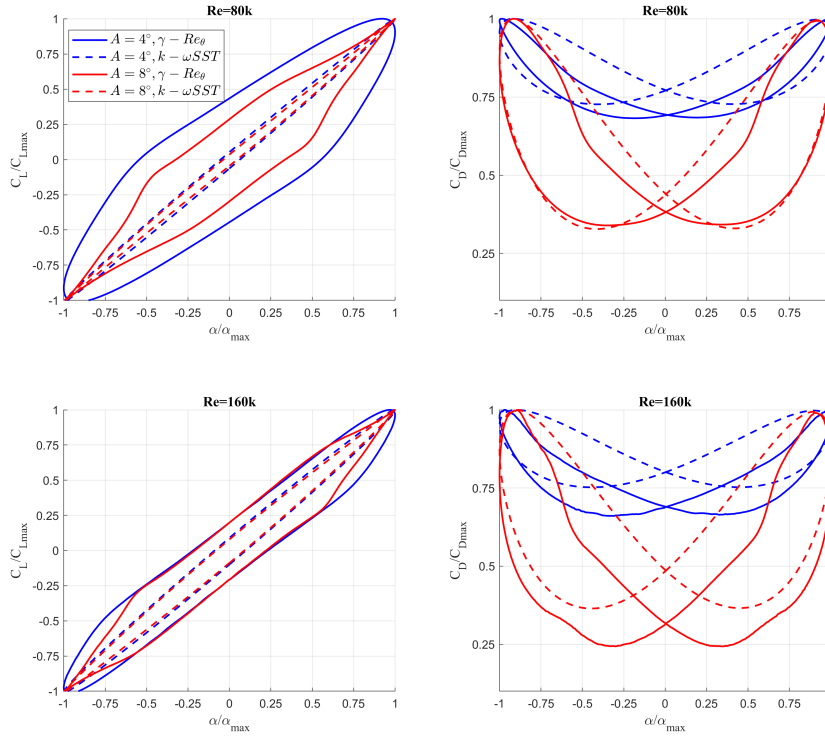


**Figure 18** Normalized lift coefficient ( $C_L/C_{L,\max}$ ) and drag coefficient ( $C_D/C_{D,\max}$ ) as a function of normalized angle of attack ( $\alpha/\alpha_{\max}$ ) for Reynolds numbers  $Re = 80k$  and  $Re = 160k$ , and pitching amplitudes  $A = 4^\circ$  and  $A = 8^\circ$ . The top row compares  $Re = 80k$ , while the bottom row compares  $Re = 160k$ .

## 4 Conclusion

The primary objective of this study was to analyze the aerodynamic loads on the symmetric, thick NACA 0018 airfoil under pitching motion at low Reynolds numbers. The oscillation frequencies were set to 1 and 2 Hz, while the amplitudes were 4 and 8 degrees. Additionally, steady-state simulations for a clean airfoil were conducted for angles of attack up to 20 degrees to validate the numerical model. The main observations from this study are as follows:

1. The four-equation  $\gamma - Re_\theta$  turbulence model performed significantly better in predicting steady aerodynamic characteristics at higher Reynolds numbers. At lower Reynolds numbers, as the flow becomes laminar, the model struggles to accurately capture the  $C_L$  curve, even at small angles of attack. For more accurate representation under these conditions, three-dimensional modeling and at least LES approaches are

required. Nevertheless, the results from the Transition SST model are more physical compared to classical turbulence models.

2. The classical two-equation  $k - \omega$  SST turbulence model, which assumes a fully turbulent boundary layer, does not produce any nonlinearities in the lift force characteristics for angles of attack below the critical angle. Consequently, laminar boundary layer separation effects are absent. Interestingly, the difference between the drag coefficient predicted by this model and the experimental results decreases as the Reynolds number decreases.

3. The XFOIL approach, which also models laminar-to-turbulent transition, overestimates the lift coefficients, although the drag coefficients are acceptable for moderate angles of attack. Calibration is required when using XFOIL for thick airfoils.

4. The dynamic characteristics of the airfoil are strongly influenced by both the oscillation amplitude and the reduced frequency. At lower Reynolds numbers, earlier boundary layer separation leads to an increase in the amplitude of the lift coefficient for small oscillation amplitudes.

5. Laminar separation bubbles cause significant hysteresis in the lift coefficient at low angles of attack and lead to notable oscillations in aerodynamic forces. For the  $C_L$  characteristics obtained using the  $k - \omega$  SST model, oscillations are nearly absent, and the hysteresis in  $C_L$  is minimal.

6. Both the Reynolds number and the oscillation amplitude and frequency significantly affect the drag coefficient, as shown by both turbulence models used in this study. Specifically, when the Reynolds number is halved from 160k, the drag coefficient decreases substantially. Furthermore, increasing the amplitude at the same Reynolds number significantly reduces the ratio of minimum to maximum drag coefficient ( $C_D/C_{Dmax}$ ).

7. An increase in the oscillation frequency from 1 Hz to 2 Hz demonstrated a significant reduction in the oscillations of the aerodynamic force components at a Reynolds number of 80k.

8. The pitching motion of the NACA 0018 airfoil induces notable hysteresis in the transition location, even at small amplitudes.

9. The study demonstrates that the similarity in aerodynamic loads obtained from the  $\gamma - Re_\theta$  and  $k - \omega$  SST models can be partially explained by the reduced impact of laminar separation bubbles at the tested conditions. The results highlight that the  $\gamma - Re_\theta$  model provides consistent performance with negligible oscillations, particularly at lower frequencies and Reynolds numbers, while the  $k - \omega$  SST model shows improved agreement with the  $\gamma - Re_\theta$  model at higher Reynolds numbers. These findings emphasize the importance of considering laminar separation bubble dynamics and Reynolds number effects when selecting turbulence models for simulating pitching airfoils, especially in applications involving vertical-axis wind turbines.

These findings provide new insights into the aerodynamic performance of thick airfoils at low Reynolds numbers and demonstrate the importance of turbulence modeling in capturing flow physics accurately.

## Declarations

### Funding

This work was supported by the POB Energy program at Warsaw University of Technology, under the Excellence Initiative: Research University (IDUB) (Grant No. 1820/355/Z01/POB7/2021). Computational resources were provided by the Interdisciplinary Centre for Mathematical and Computational Modelling at the University of Warsaw (ICM UW) through computational allocations no. G93-1588 and G94-1718.

### Conflict of Interest

The authors declare no conflict of interest.

### Ethics Approval and Consent to Participate

Not applicable.

### Consent for Publication

All authors consent to the publication of this manuscript.

### Data Availability

The datasets generated and analyzed during the current study are available from the corresponding author on reasonable request.

### Data Availability

Not applicable.

### Materials Availability

Not applicable.

### Author Contributions

Krzysztof Rogowski conceptualized and supervised the research. Maciej Śledziewski and Krzysztof Rogowski performed numerical simulations. Jan Michna analyzed the results and prepared the figures. All authors contributed to writing and reviewing the manuscript.

## References

- [1] Kojima, R., Nonomura, T., Oyama, A., Fujii, K.: Large-eddy simulation of low-reynolds-number flow over thick and thin naca airfoils. *Journal of Aircraft* **50**(1), 187–196 (2013) <https://doi.org/10.2514/1.C031849>

- [2] Anyoji, M., Nonomura, T., Aono, H., Oyama, A., Fujii, K., Nagai, H., Asai, K.: Computational and experimental analysis of a high-performance airfoil under low-reynolds-number flow condition. *Journal of Aircraft* **51**(6), 1864–1872 (2014) <https://doi.org/10.2514/1.C032553>
- [3] Fujino, K., Suzuki, K.: Mechanism of periodic oscillation in low-reynolds-number buffet around an airfoil at angle of attack 0. *Physics of Fluids* **36**(4) (2024) <https://doi.org/10.1063/5.0201260>
- [4] Li, J., Nagata, K., Watanabe, T.: Aerodynamic characteristics of airfoils with fractal structures in low-reynolds-number regime. *CEAS Aeronautical Journal*, 1–16 (2024) <https://doi.org/10.1007/s13272-024-00777-z>
- [5] Jimenez-Soler, P., Lichota, P.: Mitigating sensor quality issues in uav system identification through wavelet decomposition. *Bulletin of the Polish Academy of Sciences Technical Sciences*, 152216–152216 (2025) <https://doi.org/10.24425/bpasts.2024.152216>
- [6] Tescione, G., Ragni, D., He, C., Ferreira, C.S., Van Bussel, G.: Near wake flow analysis of a vertical axis wind turbine by stereoscopic particle image velocimetry. *Renewable Energy* **70**, 47–61 (2014) <https://doi.org/10.1016/j.renene.2014.02.042>
- [7] Rogowski, K., Michna, J., Ferreira, C.: Numerical analysis of aerodynamic performance of a fixed-pitch vertical axis wind turbine rotor **18**(6), 97–109 (2024) <https://doi.org/10.12913/22998624/191128>
- [8] Huang, M., Sciacchitano, A., Ferreira, C.: On the wake deflection of vertical axis wind turbines by pitched blades. *Wind Energy* **26**(4), 365–387 (2023) <https://doi.org/10.1002/we.2803>
- [9] Huang, M.: Wake and wind farm aerodynamics of vertical axis wind turbines ph. d. PhD thesis, thesis Delft University of Technology (2023). <https://doi.org/10.4233/uuid:14619578-e44f-45bb-a213-a9d179a54264>
- [10] Rogowski, K.: Cfd computation of the h-darrieus wind turbine—the impact of the rotating shaft on the rotor performance. *Energies* **12**(13), 2506 (2019) <https://doi.org/10.3390/en12132506>
- [11] Michna, J., Rogowski, K.: Numerical study of the effect of the reynolds number and the turbulence intensity on the performance of the naca 0018 airfoil at the low reynolds number regime. *Processes* **10**(5), 1004 (2022) <https://doi.org/10.3390/pr10051004>
- [12] Istvan, M.S., Yarusevych, S.: Effects of free-stream turbulence intensity on transition in a laminar separation bubble formed over an airfoil. *Experiments in Fluids* **59**(3), 52 (2018) <https://doi.org/10.1007/s00348-018-2511-6>

- [13] Kawai, S., Asada, K., Oyama, A.: Freestream turbulence effects in large-eddy simulations of laminar separation bubble. *Journal of Aircraft* **60**(5), 1721–1727 (2023) <https://doi.org/10.2514/1.C037058>
- [14] Melani, P.F., Balduzzi, F., Ferrara, G., Bianchini, A.: An annotated database of low reynolds aerodynamic coefficients for the naca0018 airfoil. In: *AIP Conference Proceedings*, vol. 2191 (2019). <https://doi.org/10.2514/6.2015-0723> . AIP Publishing
- [15] Langtry, R.B.: A correlation-based transition model using local variables for unstructured parallelized cfd codes (2006) <https://doi.org/10.18419/opus-1705>
- [16] Divakaran, U., Ramesh, A., Mohammad, A., Velamati, R.K.: Effect of helix angle on the performance of helical vertical axis wind turbine. *Energies* **14**(2), 393 (2021) <https://doi.org/10.3390/en14020393>
- [17] Smith, A.M.O.: Transition, pressure gradient and stability theory. Douglas Aircraft Co., Report ES 26388 (1956)
- [18] Bianchini, A., Balduzzi, F., Rainbird, J.M., Peiro, J., Graham, J.M.R., Ferrara, G., Ferrari, L.: An experimental and numerical assessment of airfoil polars for use in darrieus wind turbines: Part 1—flow curvature effects. In: *Turbo Expo: Power for Land, Sea, and Air*, vol. 56802, pp. 009–46006 (2015). <https://doi.org/10.1115/1.4031269> . American Society of Mechanical Engineers
- [19] Theodorsen, T.: General theory of aerodynamic instability and the mechanism of flutter. Technical Report NACA-TR-496, National Advisory Committee for Aeronautics (NACA) (1979)
- [20] Glauert, H.: The force and moment on an oscillating aerofoil. *Vorträge aus dem Gebiete der Aerodynamik und verwandter Gebiete: Aachen 1929*, 88–95 (1930)
- [21] Badrya, C., Govindarajan, B., Chopra, I.: Basic understanding of unsteady airfoil characteristics at low reynolds number (10<sup>4</sup>–10<sup>5</sup>). *Department of Aerospace Engineering, University of Maryland* **55**(2), 1–12 (2018) <https://doi.org/10.2514/1.C034415>
- [22] Leishman, G.J.: *Principles of Helicopter Aerodynamics with CD Extra*. Cambridge university press, ??? (2006)
- [23] Mikkelsen, R., Bak, C., Gaunaa, M., Fischer, A., Olsen, A.S., Ildvedsen, S., Beckerlee, J.: Dynamic stall measurements of a harmonic pitching naca63-018 airfoil at high reynolds numbers. In: *Journal of Physics: Conference Series*, vol. 2767, p. 022067 (2024). <https://doi.org/10.1088/1742-6596/2767/2/022067> . IOP Publishing
- [24] Stevens, P., Babinsky, H.: Experiments to investigate lift production mechanisms

- on pitching flat plates. *Experiments in Fluids* **58**(1), 7 (2017) <https://doi.org/10.1007/s00348-016-2290-x>
- [25] Brunton, S., Rowley, C.: Modeling the unsteady aerodynamic forces on small-scale wings. In: 47th AIAA Aerospace Sciences Meeting Including the New Horizons Forum and Aerospace Exposition, p. 1127 (2009). <https://doi.org/10.2514/6.2009-1127>
- [26] Kang, C.-k., Aono, H., Sik Baik, Y., Bernal, L.P., Shyy, W.: Fluid dynamics of pitching and plunging flat plate at intermediate reynolds numbers. *AIAA journal* **51**(2), 315–329 (2013) <https://doi.org/10.2514/1.J051593>
- [27] Moriche, M., Flores, O., García-Villalba, M.: Three-dimensional instabilities in the wake of a flapping wing at low reynolds number. *International Journal of Heat and Fluid Flow* **62**, 44–55 (2016) <https://doi.org/10.1016/j.ijheatfluidflow.2016.06.015>
- [28] Rogowski, K., Mikkelsen, R.F., Michna, J., Wiśniewski, J.: Aerodynamic performance analysis of naca 0018 airfoil at low reynolds numbers in a low-turbulence wind tunnel. *Advances in Science and Technology. Research Journal* **19**(2) (2025) <https://doi.org/10.12913/22998624/195556>
- [29] Vitagliano, P.L., Minervino, M., Quagliarella, D., Catalano, P.: A conservative sliding mesh coupling procedure for u-rans flow simulations. *Aircraft Engineering and Aerospace Technology: An International Journal* **88**(1), 151–158 (2016) <https://doi.org/10.1108/AEAT-09-2014-0135>
- [30] ANSYS Inc.: ANSYS Fluent User’s Guide, Release 2024. (2024). Available at: <https://www.ansys.com>
- [31] Menter, F.R., Langtry, R.B., Likki, S., Suzen, Y.B., Huang, P., Völker, S.: A correlation-based transition model using local variables—part i: model formulation. *Journal of turbomachinery* **128**(3), 413–422 (2006) <https://doi.org/10.1115/1.2184352>
- [32] Rogowski, K., Michna, J., Mikkelsen, R.F., Ferreira, C.: Impact of zigzag tape on blade loads and aerodynamic wake in a vertical axis wind turbine: A delft vawt case study (2025) <https://doi.org/10.2139/ssrn.5059693> . Available at SSRN: <https://ssrn.com/abstract=5059693>
- [33] Mendoza, V., Bachant, P., Ferreira, C., Goude, A.: Near-wake flow simulation of a vertical axis turbine using an actuator line model. *Wind Energy* **22**(2), 171–188 (2019) <https://doi.org/10.1002/we.2277>
- [34] Rezaeiha, A., Kalkman, I., Blocken, B.: Cfd simulation of a vertical axis wind turbine operating at a moderate tip speed ratio: Guidelines for minimum domain size and azimuthal increment. *Renewable energy* **107**, 373–385 (2017) <https://doi.org/10.1016/j.renene.2017.05.030>

[doi.org/10.1016/j.apenergy.2017.03.128](https://doi.org/10.1016/j.apenergy.2017.03.128)

- [35] Rezaeiha, A., Montazeri, H., Blocken, B.: On the accuracy of turbulence models for cfd simulations of vertical axis wind turbines. *Energy* **180**, 838–857 (2019)  
<https://doi.org/10.1016/j.energy.2019.05.053>
- [36] Damiola, L., Siddiqui, M.F., Runacres, M.C., De Troyer, T.: Influence of free-stream turbulence intensity on static and dynamic stall of a naca 0018 aerofoil. *Journal of Wind Engineering and Industrial Aerodynamics* **232**, 105270 (2023)  
<https://doi.org/10.1016/j.jweia.2022.105270>